

RAIDER: Rapid, anatomy-independent, deep learning-based PDFF and R_2^* estimation using magnitude-only signals, dual neural networks and training data distribution design

Timothy JP Bray^{1,2,3}, Giulio V Minore³, Alan Bainbridge⁴, Louis Dwyer-Hemmings^{1,2,3}, Stuart A Taylor^{1,2}, Margaret A Hall-Craggs^{1,2}, Hui Zhang³

1 Centre for Medical Imaging, University College London, UK

2 Department of Imaging, University College London Hospital, UK

3 The Hawkes Institute, University College London, UK

4 Department of Medical Physics, University College London Hospital, UK

Abstract

There has been recent interest in the use of magnitude-based fitting methods for estimating proton density fat fraction (PDFF) and R_2^* from chemical shift-encoded MRI data, since these methods can still be used when complex-based methods fail or when phase data are inaccessible or unreliable (such as in multicentre trials, low resource settings, preclinical imaging and national cohort datasets), and may also be used as a final processing step with complex-based methods. However, conventional fitting techniques are computationally expensive. Deep learning (DL)-based methods promise to accelerate parameter estimation, but there are no existing deep learning methods for voxelwise CSE-MRI parameter estimation. Here, we show that a naive voxelwise MLP implementation suffers from poor performance because multiple parameter values can produce similar signals (degeneracy), potentially accounting for this gap in the literature. To address this problem and realise the potential acceleration offered by MLP-based parameter estimation, we propose RAIDER, a voxelwise method for rapid, anatomy-independent deep learning-based PDFF and R_2^* estimation using multi-echo magnitude-data. RAIDER utilises two neural networks, each with a separately-designed training data distribution, to deal with degeneracy and thus realise the benefits of an MLP-based approach, with a 400-fold to 2800-fold acceleration (meaning that processing takes just seconds, rather than minutes or hours). Our code is available at <https://github.com/TJPBray/DixonDL>.

Keywords

Machine Learning, Quantitative Magnetic Resonance Imaging

Article informations

©2025 Timothy Bray and Hui Zhang. License: CC-BY 4.0

Corresponding author: t.bray@ucl.ac.uk

1. Introduction

Chemical shift-encoded MRI (CSE-MRI) is a reliable, fast method for quantifying proton density fat fraction (PDFF) in a wide variety of organs and disease states (Reeder et al., 2004, 2005; Hernando et al., 2008; Liu et al., 2007; Nouredin et al., 2013; Bray et al., 2018b). PDFF measurements are now established for the measurement of steatosis in liver (Nouredin et al., 2013), and are also increasingly used for other organs including pancreas (Yoon et al., 2016; Kuhn et al., 2015), muscle (Morrow et al., 2016) and bone marrow (Bray et al., 2018a; Lati-foltojar et al., 2017; Messiou et al., 2019). CSE-MRI most commonly utilises multi-echo gradient echo acquisitions, meaning that R_2^* measurements can be extracted from the

same acquisition, providing additional quantitative information on iron or calcium. PDFF and R_2^* measurements estimated using gradient echo acquisitions therefore offer flexible biomarkers informing on a wide variety of pathological processes. The speed of the underpinning acquisitions means that these biomarkers can also be acquired in the context of whole body MRI (WB-MRI), which is becoming an important tool for lesion characterisation and disease staging in cancer (Messiou et al., 2019; Taylor et al., 2019; Costelloe et al., 2012), amongst other applications such as the assessment of inflammatory arthritis (Choida et al., 2022, 2024).

From a signal processing perspective, the central challenge of CSE-MRI is to disentangle or separate the signals

arising from water and fat. This is challenging because the signal arising from water-dominant and fat-dominant tissues is very similar, giving rise to the so-called ‘fat-water ambiguity’ problem. The prevailing approach to solving this problem has been to use the phase of the complex signal in order to separate water and fat: with complex signal-based methods, water-dominant and fat-dominant tissues can be distinguished on the basis of their phase, so long as the contribution to the phase from main magnetic field B_0 can be estimated accurately and therefore separated from the phase arising due to chemical shift (Reeder et al., 2004, 2005; Hernando et al., 2008; Liu et al., 2007; Nouredin et al., 2013).

However, although these complex signal-based methods can be very effective, in some situations complex data (and/or expensive vendor-supplied software packages for $PDFF$ estimation) may be unreliable or not available, creating a substantial barrier to the use of CSE-MRI. This problem applies to various scenarios including multi-centre studies (Bainbridge et al., 2020; Wong et al., 2023; Waddell et al., 2022; Losev et al., 2024), low resource clinical and research settings (Murali et al., 2022), preclinical imaging (Ghimire et al., 2025) and when retrospectively analysing existing datasets such as the UK biobank and German national cohort study (Littlejohns et al., 2020; Consortium, 2014).

As a result of these limitations, a different class of methods using only the magnitude of the signal (i.e. where the signal phase is discarded) for parameter estimation have been developed. As phase information is not available to these methods, they require a different source of information to resolve fat-water ambiguity. Recently, the development of the MAGO and MAGORINO methods demonstrated that this ambiguity could be resolved on the basis of subtle differences in the oscillations of the magnitude signal over multiple echoes (Triay Bagur et al., 2018; Bray et al., 2022). In addition to being usable in situations where complex data and/or expensive vendor-supplied software packages are not available, these methods also avoid phase errors which can induce bias when fitting with complex data, meaning that they may be more accurate and robust than complex signal-based techniques in a real-world setting. Related to these advantages, the MAGO technique (not developed by these authors) has achieved regulatory clearance within the LiverMultiscan package (Perspectum, Oxford) and is increasingly being used in clinical trials (Wong et al., 2023; Waddell et al., 2022; Losev et al., 2024). Importantly, magnitude-based fitting is also commonly used as a final processing step even in complex fitting pipelines (Hernando et al., 2017), and is the central fitting method used in the Siemens qDixon package (Zhong et al., 2014). There has also been interest in using magnitude-fitting as a first processing step in order to improve estimation of

B_0 inhomogeneity, with a view to performing quantitative susceptibility mapping (QSM) (Triay Bagur et al., 2023).

These developments suggest that magnitude-based fitting will continue to have a crucial role in CSE-MRI processing. However, these methods carry a substantial computational cost, due to the iterative nature of the algorithms as well as the need to perform fitting with nonlinear least squares several times - with different start points - in order to ensure that the correct likelihood maximum / error minimum is found (Triay Bagur et al., 2018; Bray et al., 2022). This increases the time, human resource and funding required to use these techniques, limiting their use in research settings and in clinical practice.

A promising approach to reducing this computational cost is to use deep learning for parameter estimation: this has the advantage that computational cost is front-loaded: training can be performed in advance, before images are acquired, and the computational resources needed to actually process those images are typically much less than with conventional fitting (Barbieri et al., 2019; Epstein et al., 2024; Gyori et al., 2021). However, to our knowledge there is no existing voxel-independent deep learning-based method for $PDFF$ and R_2^* fitting of multi-echo CSE-MRI data.

To address this problem, here we develop a novel approach using multiple multilayer perceptrons (MLPs) for $PDFF$ and R_2^* estimation from multi-echo magnitude signals. We first identify a crucial problem with a ‘naive’ single MLP implementation, related to model degeneracy: the network performs poorly because multiple combinations of parameter values can produce very similar signals. To solve this degeneracy problem, we introduce a novel method whereby two MLPs, each trained separately with a restricted training distribution, are used to avoid degeneracy and thus estimate these parameters. The new method is referred to as RAIDER: **rapid, anatomy-independent deep learning-based CSE-MRI**.

2. Theory and related works

2.1 Tissue and noise models

A full description of the tissue and noise models used in this work is given in Bray et al. (2022); the key tissue and noise models are briefly summarised here.

With a gradient echo-based CSE-MRI acquisition, the noise-free complex signal S acquired at echo time t can be modelled as:

$$S(t|S_0, PDFF, R_2^*, f_B) = S_0 \left((1 - PDFF) + PDFF \sum_{q=1}^Q r_m e^{i2\pi f_{F,q} t} \right) e^{i2\pi f_B t} e^{-tR_2^*} \quad (1)$$

where S_0 and $PDFF$ are the theoretical signal intensity at $t=0$ and proton density fat fraction respectively, $f_{F,q}$ is the frequency of each spectral fat component, r_q is the relative amplitude of each spectral fat component, Q is the total number of spectral fat components, f_B is the frequency offset due to B_0 inhomogeneity and $R_2^* = 1/T_2^*$ is an unknown relaxation constant. It is conventional to assume that the relative amplitudes and frequency offsets of each fat component are known *a priori*; therefore the unknown parameters are S_0 , $PDFF$, f_B and R_2^* . Note that this formulation slightly differs from that in Bray et al. (2022), where the parameters included ρ_f and ρ_w rather than S_0 and $PDFF$. The current formulation has been chosen as it allows a more convenient estimation of S_0 after the DL-based estimation of $PDFF$ and R_2^* , as detailed in Section 3.1.4.

In the presence of Gaussian noise (present in both real and imaginary channels), the log likelihood for a set of predicted noise-free signals, given the measured noisy signals, is given by

$$\log L(\{S_i\}, \sigma^2 | \{S'_i\}) = -n \log(\sqrt{2\pi\sigma^2}) - \sum_{i=1}^n \frac{|S'_i - S_i|^2}{2\sigma^2} \quad (2)$$

where $\{S_i\}$ is the set of predicted signals based on the parameter estimates, $\{S'_i\}$ is the set of measured signals, σ^2 is the variance of the Gaussian distribution for the noise, n is the number of measurements (double the number of echo times for complex data, or the number of echo times for magnitude data).

For the signal magnitude, the noise-free signal in Eqn (1) becomes

$$M(t|S_0, PDFF, R_2^*) = S_0 \left| (1 - PDFF) + PDFF \sum_{q=1}^Q r_q e^{i2\pi f_{F,q}t} \right| e^{-tR_2^*} \quad (3)$$

with only three unknown parameters: S_0 , $PDFF$, and R_2^* .

Taking the magnitude dictates that each noisy measurement now has a Rician distribution. The log likelihood for a set of predicted noise-free signals becomes

$$\log L(\{M_i\}, \sigma^2 | \{M'_i\}) = \sum_{i=1}^n \left[\log \frac{M'_i}{\sigma^2} - \frac{M_i'^2 + M_i^2}{2\sigma^2} + \log I_0\left(\frac{M'_i M_i}{\sigma^2}\right) \right] \quad (4)$$

where $\{M'_i\}$ is the set of measured magnitude signals at different echo times, $\{M_i\}$ is the corresponding set of predicted magnitude signals and I_0 is the 0^{th} order modified Bessel function of the first kind.

2.2 Dual optima problem and the source of degeneracy in CSE-MRI

With magnitude-based fitting, the likelihood functions defined in Eqns (2) and (4) have two optima: one 'true' solution corresponding closely to the ground truth and one incorrect 'swapped' solution with a $PDFF$ value at the opposite end of the range (i.e. with a $PDFF$ value close to 1 - $PDFF$) (Fig. 1). This creates a source of degeneracy - for a given set of signals, there are two candidate solutions which have very similar likelihood. The MAGO and MAGORINO methods used two-point search to ensure that both optima are explored (Triay Bagur et al., 2018; Bray et al., 2022), and thus ensure that the global optimum would correspond to the true solution. However, this degeneracy can create a problem for deep learning, as outlined in Section 2.4.

Note that there is a stationary or 'switching' point close to 60% in the $PDFF$ dimension, below which the initial guesses are likely to converge to the low $PDFF$ solution and above which the initial guesses are likely to converge to the high $PDFF$ solution (in 2D this is a saddle or min-max point) - this switching point is shown in Figure 1. This is relevant to the degeneracy problem discussed in Section 2.4.

2.3 Parameter estimation with deep learning

The use of neural networks for curve fitting was first proposed by Bishop and Roach (1992), and has become increasingly widely used for qMRI parameter estimation with the arrival of deep learning. Unlike with conventional fitting, which iteratively finds the points on an objective function at which error is minimized / likelihood is maximised, a deep neural network is trained to directly map a single voxel's signal to its corresponding qMRI parameters (Golgov et al., 2016). The unknowns in this model are thus the network weights rather than the parameters in the signal model; the training procedure aims to find the values of these weights that minimise the distance between the predicted parameter estimates and the training labels in the training dataset. Once the network has been trained, parameter estimation for any data can be achieved in a single shot by inputting the data to the network. This effectively front-loads the computational cost and means that the cost at the time the network is applied is dramatically reduced compared to conventional fitting.

2.4 Degeneracy in deep learning

Bishop noted that neural networks were able to represent one-to-one and many-to-one mappings, but could not represent one-to-many ('multivalued') mappings (Bishop and Roach, 1992). This problem was referred to by Bishop as an 'ambiguity phenomenon' and is referred to here as de-

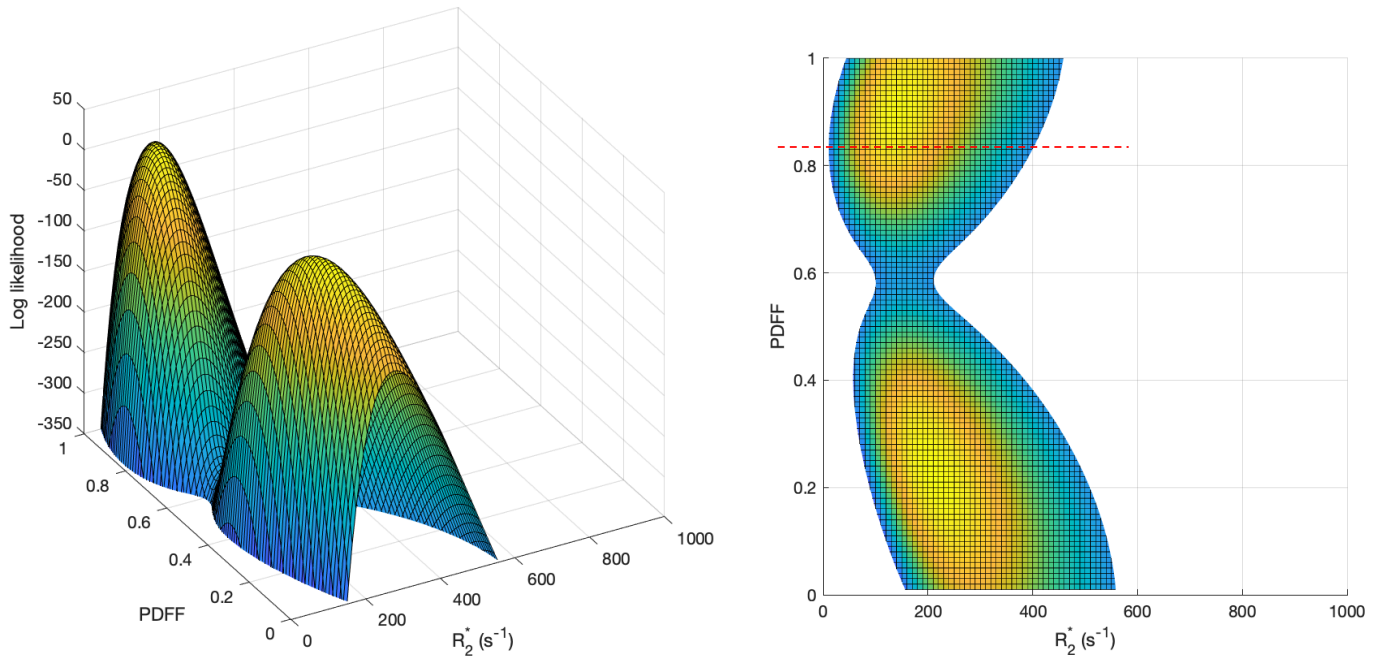


Figure 1: Illustration of how the presence of two likelihood optima leads to degeneracy in CSE-MRI. The Rician log likelihood is shown as a function of PDFF and R_2^* for a voxel with PDFF = 0.2 and $R_2^* = 200 \text{ s}^{-1}$ (oblique view, left, and top-down view, right). There are two optima, occurring at low PDFF (in this case this corresponds to the true solution) and high PDFF (in this case this corresponds to the swapped solution). This creates a source of degeneracy - for a given set of signals, there are two candidate solutions which have very similar likelihood, creating a ‘one-to-many’ problem which traditionally deep learning approaches are poorly equipped to solve. The switching line at PDFF = 0.58 (explained in Section 3.2.2) is shown as a dotted red line.

generacy. In Bishop’s experiments, the quality of the neural network fits was found to be very poor in regions of parameter space where this degeneracy problem occurred. Guerri et al. recently provided further theoretical insights into this problem, showing that, in the presence of degenerate samples during supervised training, the function learned by the neural network will map the degenerate signal to the empirical mean of tissue properties over the degenerate subset (Guerreri et al., 2023). In other words, in this situation the network does not learn either of the correct solutions.

A problem of this type is encountered in CSE-MRI, where a one-to-many problem exists because there are two sets of parameter values (the ‘true’ solution and the ‘swapped’ solution) which correspond to very similar signals. This problem is relatively minor at low R_2^* but becomes more severe at higher R_2^* and/or lower SNR, as the water and fat peaks become broader and therefore more difficult to resolve (Bray et al., 2022). Bishop suggested that, in cases where there were multiple potential solutions for a given input, this problem could be solved by excluding a region of the output space (Bishop and Roach, 1992). However, this approach assumes that one region of output space can

be discarded on the basis that it is unlikely to occur in experiments. With CSE-MRI, this is not a satisfactory solution because both low PDFF and high PDFF values can be present in real tissue.

To address this problem, we propose dividing the parameter space into two parts, in such a way that one network can be trained on the first part of parameter space, and another network can be trained on the second part of parameter space, without degeneracy. Specifically, we divide the parameter space into low PDFF regions, with PDFF values below the switching line, and high PDFF regions, with PDFF values above the switching line. The value of the switching line is chosen by inspecting the objective functions shown in Figure 1 to determine the location of the switching point in the PDFF dimension, as described previously (Triay Bagur et al., 2018; Bray et al., 2022); further implementation details are provided in Section 3.2.2.

By dividing the training distribution in this way and training separate networks, we create two networks that are each accurate within the region of parameter space on which they are trained. The correct output from the two networks can then be chosen based on the difference in

likelihood (as defined in Eqn (4)) between the two solutions. Our approach is analogous to conventional fitting approaches where different optima are explored using multiple start points (Triay Bagur et al., 2018; Bray et al., 2022), but carries an essentially negligible computational cost.

3. Methods

3.1 Network

An overview of the training procedures for single and dual network approaches and the inference procedure for the dual network approach is provided schematically in Figure 2; detail on, and justification of, the individual elements within this schematic is provided in the following subsections.

3.1.1 Normalization using single peak approximation of S_0

Unlike existing voxelwise DL methods focusing on diffusion MRI (Karimi, 2024), where $b=0$ is directly measured, with CSE-MRI we do not have access to a signal measurement at $TE=0$, meaning that a simple normalization method is not readily available. To address this problem, and to make network predictions robust to variations in signal intensity (i.e. variations in S_0), we developed a novel normalization procedure: the multi-echo signals were normalized by a rough approximation of S_0 before being inputted to the network(s). This rough S_0 approximation, denoted \hat{S}_0 , was obtained by taking the measured signal for the two echo times closest to the first and second ‘in-phase’ echo times (assuming a single peak model), calculating the decay between these echo times (assuming monoexponential decay) and then extrapolating back to $t = 0$ using a log-linear fit. Note that these chosen echo times do not vary between voxels but are protocol-specific. To ensure that this procedure did not result in an \hat{S}_0 lower than the maximum measured signal intensity, if $\hat{S}_0 < \max M(t)$, then \hat{S}_0 was set to be equal to $\max M(t)$.

This step was applied both during training and at inference (see Figure 2). Note that this step is not expected to produce accurate parameter estimates, and it is anticipated that the network learns to compensate for inaccuracies in this step. Note also that a further, updated estimate of S_0 is obtained after the network predictions, as detailed in 3.1.4.

3.1.2 Network architecture

We used a simple network design consisting of five fully-connected layers, with first four having the same number of nodes as the number of signal measurements (i.e. echo times), and the fifth (output) layer having a node for each

model parameter (i.e. one output node for PDFF and one for R_2^*), with exponential linear unit (ELU) activation functions (Clevert et al., 2015; Epstein et al., 2024). This design is similar to Barbieri et al. (2019) and Epstein et al. (2024), but uses five layers rather than three to increase network capacity.

To ensure that these networks had sufficient capacity, we also implemented several deeper and wider networks, the largest of which had fifty times as many nodes as the number of signal measurements in each fully connected hidden layer and twelve rather than five fully connected layers (11 hidden layers and one output layer). The capacity of both standard and larger networks was examined in experiments analogous to those described in 3.2 but using noise-free training data, as detailed in Appendix A. These results (taken together with the rest of the experiments) show that larger networks offer a performance benefit, due to greater capacity, in the noise-free setting but that the smaller networks show equivalent performance when training and evaluation are performed in the presence of noise. The finding that greater capacity is needed for noise-free data is consistent with Gyori et al. (2021). The networks were implemented in Matlab 2021b using the MATLAB Deep Learning toolbox.

3.1.3 Network training

The network was trained in a supervised fashion using entirely simulated data based on the signal models highlighted in Section 2.1. First, parameter values (labels) were randomly drawn from PDFF / R_2^* parameter space (using a uniform distribution within the defined parameter ranges to minimise bias (Gyori et al., 2021)); the corresponding simulated signal intensities were then simulated, and Rician noise was added with SNR values randomly sampled from a uniform distribution (Mastropietro et al., 2019) between 20 (very low SNR) and 120 (very high SNR, designed to exceed the upper end of the SNR range expected in vivo (Triay Bagur et al., 2018; Bray et al., 2022)). Normalisation was performed as detailed in 3.1.1 and as shown in Figure 2.

Training was performed using an Adam optimiser with learning rate 0.001 (Epstein et al., 2024), minibatch size 32, validation patience 50 (more conservative than Barbieri et al. (2019), who used validation patience of 10). Additionally, to enable effective training of the larger networks, we used a piecewise learning rate schedule with drops in the learning rate by a factor of 0.2 every 5 epochs. L2 regularization was not used as the size of the synthetic dataset was deemed sufficient to minimise overfitting. Training was performed using a training dataset of 100,000 samples (Epstein et al., 2024); in the single network each network was trained on the full training dataset, whereas in dual net-

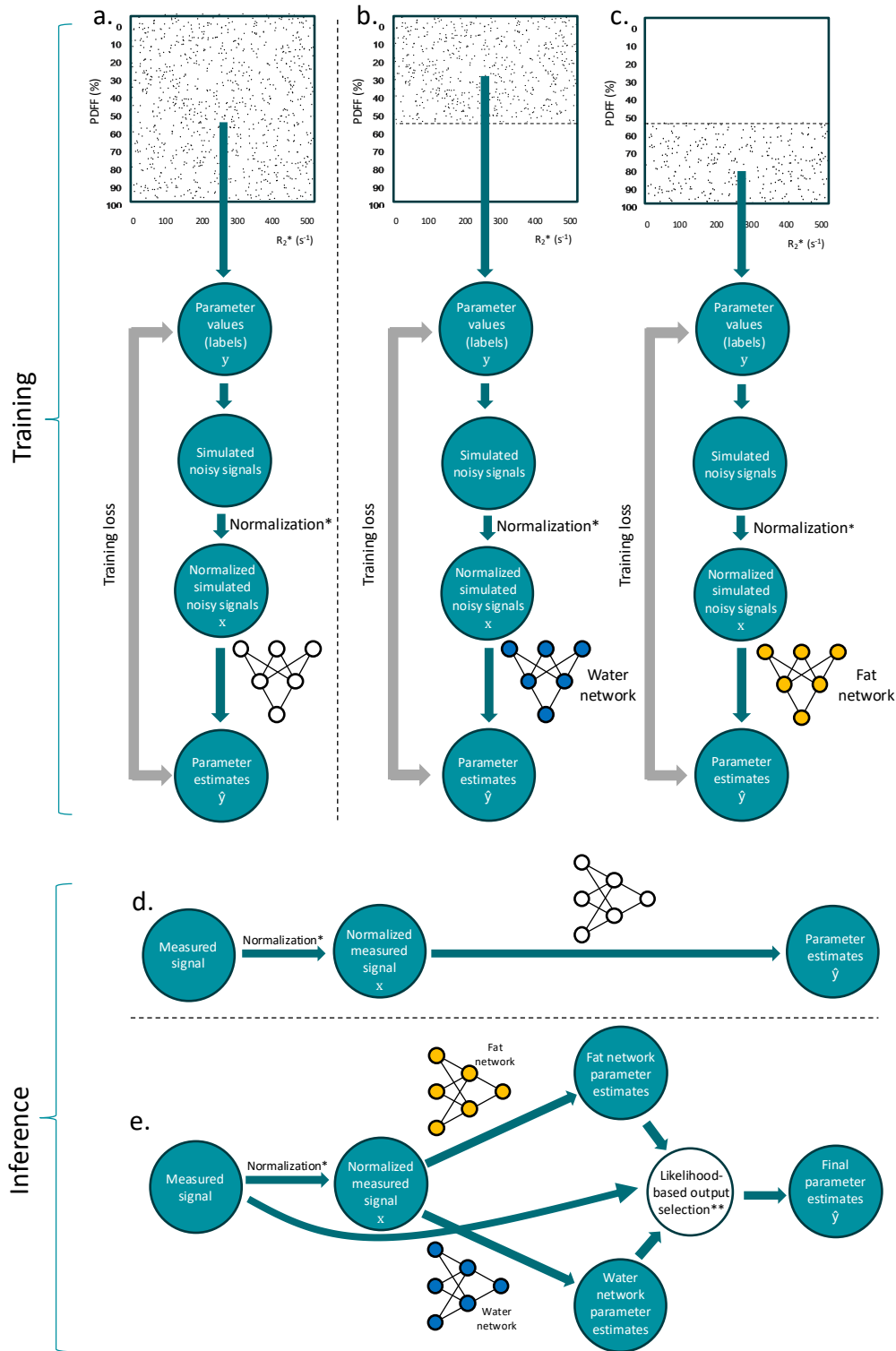


Figure 2: Training procedure for single (a) and dual (b,c) network approaches, and inference procedure for single network (d) and dual network (e) approaches. With a naive single network approach (a), one network is trained with a uniform distribution across the entire space of plausible parameter values. With the proposed approach, two separate networks are trained on separate parts of the plausible parameter space to avoid degeneracy: a 'water network' (b) is trained only on the region of parameter space below the 'switching line' (dashed line), and a 'fat network' (c) is trained only on the region of parameter space above the switching line (dashed line). At inference, for the dual network approach (e), the outputs from the two networks (fat network and water network) are treated as 'candidate' solutions; the likelihood for each candidate is calculated based on the measured signal and the one with the higher likelihood is selected (e). *Normalization is performed as detailed in 3.1.1. **The selection of either the water network or fat network output is performed as described in 3.1.4.

work case the dataset was first subdivided, as detailed in 3.2.2. In both cases, the datasets were split 80/20 between training and validation. Training was performed on an Apple iMac with 3.8-GHz, using a single central processing unit (CPU). Further details of network training are detailed in the individual experiments below. Network training took approximately 40 minutes in total (20 minutes per network) for the proposed two network approach shown in Figure 2.

3.1.4 Network output selection based on likelihood

To determine which of the two networks' predictions should be taken as the final output, the likelihood for the predicted signals from each network, given the measured signals, was compared.

To enable this, we first reformulate Eqn (3) as

$$M(t|S_0, PDFF, R_2^*) = S_0 a_t \quad (5)$$

where a_t is a known real-valued scalar quantity, calculated from the RAIDER parameter estimates using

$$a_t = |(1 - PDFF) + PDFF \sum_{q=1}^Q r_q e^{i2\pi f_{F,q} t} e^{-t R_2^*}|. \quad (6)$$

Once a_t has been calculated, a new, improved estimate of S_0 , \tilde{S}_0 , (note that this is distinct from the earlier, rough approximation \hat{S}_0) at the maximum Gaussian likelihood can be obtained using the matrix formulation

$$\mathbf{m} = \mathbf{a} \tilde{S}_0 \quad (7)$$

where \mathbf{m} is an $N \times 1$ vector of measured signal magnitudes and \mathbf{a} is an $N \times 1$ vector containing the values of a_t for each sampled echotime, and N is the total number of sampled echo times. N can be the total number of echo times acquired (we used this approach here), or a smaller number of echo times to reduce the impact of Rician noise on the estimates (we did not find any improvement in performance for this approach).

\tilde{S}_0 can be estimated using

$$\tilde{S}_0 = (\mathbf{a}^\top \mathbf{a})^{-1} \mathbf{a}^\top \mathbf{m} \quad (8)$$

Having calculated \tilde{S}_0 , the log likelihood for the predicted signals, based on the measured signals, was calculated using Eqn (4) for each of the two networks' parameter estimates, and the network predictions giving the higher likelihood were taken as the output.

To facilitate selection of the correct network output in the occasional situation that one network produced high likelihood but physically implausible parameter estimates (specifically negative R_2^* values, which could occur when a

network was exposed to signals outside its training distribution), such negative R_2^* values were deemed to be incorrect, and the outputs of the other network were selected.

3.2 Simulation Experiments

A series of simulation experiments were conducted to investigate the effect of training data distribution on the accuracy and precision of parameter estimation.

The training data was constructed by simulating noisy multi-echo signals using Eqn (3) for a range of PDFF and R_2^* values, using a typical CSE-MRI acquisition protocol with six echoes: $TE_1 = 1.152$ ms and $\Delta TE = 1.168$ ms, matching the first 3T protocol in Hernando et al. (Hernando et al., 2017). The distribution of PDFF and R_2^* values was varied for each experiment by defining regions of parameter space from which the PDFF and R_2^* values could be selected, as detailed below and in Figure 2. PDFF and R_2^* values were randomly selected within the defined region.

Performance was evaluated on a separate simulated test dataset consisting of evenly-spaced PDFF and R_2^* values across the full parameter space ($PDFF \in [0, 1]$, $R_2^* \in [0, 500] \text{ s}^{-1}$), resulting in $101 \times 21 = 2121$ combinations of parameter values. For each combination of parameter values, we simulated 100 noisy signals (at $SNR = 60$, which is typical for CSE-MRI) in order to mimic repeating the same acquisition 100 times. Performance was evaluated in terms of the bias and precision of parameter estimates, and compared against magnitude fitting with the MAGORINO algorithm (Bray et al., 2022).

3.2.1 Single network with uniform training distribution

The training dataset consisted of 100,000 sets of magnitude signals derived from randomly-generated parameter combinations with a uniform distribution in PDFF / R_2^* parameter space ($PDFF \in [0, 1]$, $R_2^* \in [0, 500] \text{ s}^{-1}$), as demonstrated in Figure 2(a).

3.2.2 Dual networks with modified training distribution

To address the effect of degeneracy on network predictions, the full dataset consisting of 100,000 signal sets was divided into two separate, smaller training datasets, as demonstrated in Figure 2(b,c):

The first network ('water network') was trained only on the low PDFF training data, i.e. with PDFF values below the switching line ($PDFF \in [0, 0.58]$, $R_2^* \in [0, 500] \text{ s}^{-1}$). Details on determining the value of the switching line are detailed in 2.4.

The second network ('fat network') was trained only on the high PDFF training data, i.e. with PDFF values above the switching line ($PDFF \in [0.58, 1]$, $R_2^* \in [0, 500] \text{ s}^{-1}$).

This approach - dividing the training data seen by the single network into two smaller datasets - (i) ensures that the dual network approach has seen the same training data as the single network approach and (ii) ensures that the parameter space sampling density is kept the same for all models.

Having trained these two networks and obtained the predictions on the test dataset, a further set of 'composite' predictions was derived by choosing the output from the two networks with the highest likelihood, as described in Section 3.1.4.

3.3 Phantom experiments

To evaluate the feasibility of DL-based fitting across a range of scanners and protocols, our method was evaluated in a publicly available multisite, multivendor, and multi-field-strength phantom data set - full details of the dataset are given in Hernando et al. (2017). Briefly, the dataset consists of fat-water mixtures with known varying fat fraction, scanned at 1.5T and 3T at six centers (two centers each for GE, Philips, and Siemens). Data acquisition was performed using each site's version of a multi-echo 3D spoiled gradient echo CSE sequence (six echo times), with two different protocols (each performed at 1.5T and 3T) performed in order to test the reproducibility across different acquisition parameters. Protocols 1 and 2 were performed at 1.5T, and protocols 3 and 4 were performed at 3T. Protocols 1 and 3 generated approximately in-phase and opposed-phased echoes, whereas protocols 2 and 4 used the shortest echoes achievable.

Deep learning-based parameter estimation was performed as described in Section 3.2.2. After generating parameter maps, fat fraction values were obtained from the individual vials of the phantom by taking the median value from ROIs placed on the individual tubes (Triay Bagur et al., 2018; Bray et al., 2022) and compared against known reference values. The performance of the networks was compared against conventional fitting.

3.4 In vivo imaging

To evaluate the feasibility of the proposed approach *in vivo*, we imaged multiple different anatomical regions in two separate subjects, on different scanners. The first subject had their pelvis and abdomen imaged on a 3T Philips Ingenia system using a multi-echo 3D spoiled gradient echo sequence with flyback gradients and monopolar readouts $TE_1 = 1.2$ ms, $\Delta TE = 1.6$ ms, six echoes, flip angle = 5° , $TR = 25$ ms, matrix size = 320×320 , and pixel spacing = 1.8×1.8 mm. The second subject had their thorax and abdomen imaged on a Siemens 3T Vida scanner using a similar acquisition with $TE_1 = 1.1$ ms, $\Delta TE = 1.1$ ms. Deep learning-based parameter estimation was performed as de-

scribed in Section 3.2.2; conventional magnitude-based fitting was performed using both Gaussian and Rician noise models, as described previously (Triay Bagur et al., 2018; Bray et al., 2022). These scans were performed with institutional review board approval (Queen Square Research Ethics Committee, London, REC 15/LO/1475), and subjects provided written informed consent.

4. Results

4.1 Simulation experiments

4.1.1 Single network with uniform training distribution

Figure 3 (left column) shows the PDFF estimation performance of a single network trained with a uniform distribution of parameter values over the full parameter space, evaluated in the presence of noise. At low PDFF, there are regions of positive error (shown in yellow in (f)) towards the right of subplots (a) and (f) (i.e. with increasing R_2^*), with estimates becoming closer to the mean PDFF. Conversely, at high PDFF, there are regions of negative error (shown in blue in f) with increasing R_2^* , again with estimates becoming closer to the mean PDFF. The precision of parameter estimates (k) also worsens with increasing R_2^* . The second column shows very little change in the results for a substantially larger network (with approximately 2500 times as many learnable parameters), indicating that the poor performance of this network is not due to lack of network capacity.

Similarly, Figure 4 (left column) shows the R_2^* estimation performance of a single network trained with a uniform distribution of parameter values over the full parameter space, evaluated in the presence of noise. At high PDFF, there are regions of positive error (shown in yellow) towards the bottom of subplot (f), and some regions of negative error (shown in blue) at low PDFF, as well as a band of negative error at high R_2^* . Again, the second column shows minimal improvement in the results for a substantially larger network.

For the full simulation experiment over 212100 signal instantiations, inference took 3.9s compared to 1649s (i.e. 27 minutes) for conventional fitting (423 fold acceleration).

4.1.2 Dual networks with modified training distribution

Water network

The third column of Figure 3 shows the PDFF estimation performance of a single network trained with a restricted, low PDFF distribution of parameter values (the 'water network'), evaluated in the presence of noise. Compared to the single network, there is a substantial improvement in performance for low PDFF values, with elimination of the high error, high variance regions at high R_2^* . However, as expected, the network fails on the high PDFF values as it

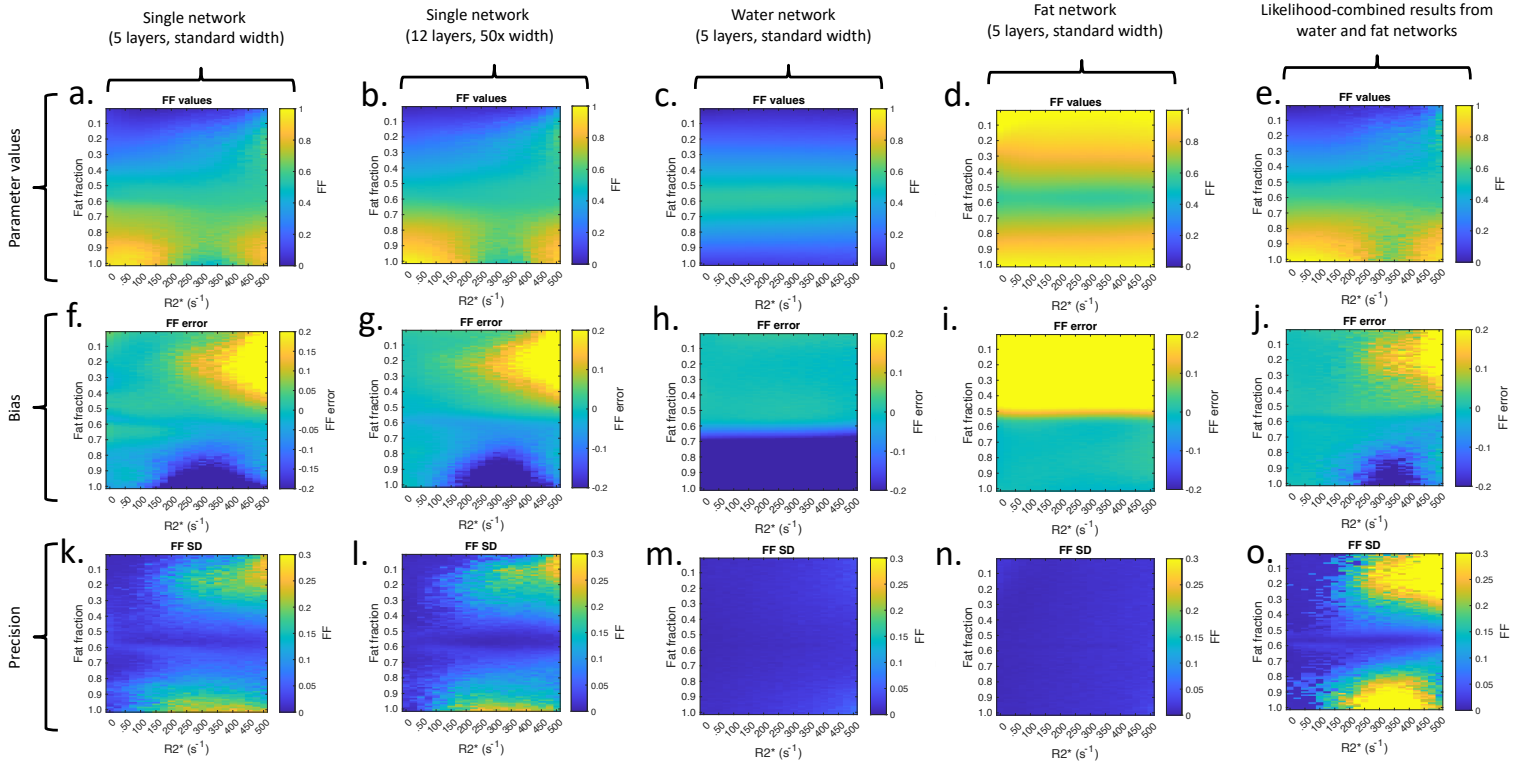


Figure 3: Improvement in PDF estimation for dual network approach compared to single network (evaluation in the presence of noise). The figure shows the performance of a single network with no restriction of training distribution ((left and second columns, using standard and larger networks respectively), individual water and fat networks (third and fourth columns) and likelihood-combined networks (right column). The parameter values are shown on the top row, bias is displayed in the middle row and parameter standard deviation is shown on the bottom row.

has not experienced this region of parameter space during training. Furthermore, (c) shows that there is a direct relationship between the bias in this region and the ground truth value, suggesting that this failure is a consequence of degeneracy.

Similarly, the third column of Figure 4 shows the R_2^* estimation performance of the same water network. Compared to the single network, there is an improvement in performance for low PDF values. However, as expected, the network fails on the high PDF values as it has not experienced this region of parameter space during training.

Fat network

The fourth column of Figure 3 shows the performance of a single network trained with a restricted, high PDF distribution of parameter values (the ‘fat network’). Compared to the single network, there is a substantial improvement in performance for high PDF values, particularly at high R_2^* . Again, as expected the network fails on the low PDF values, and (d) shows a direct relationship between the bias in this region of parameter space and the ground truth value,

suggesting degeneracy as the underlying cause.

Similarly, the fourth column of Figure 4 shows the R_2^* estimation performance of the same fat network. Compared to the single network, there is a substantial improvement in performance for high PDF values. Again, as expected, the network fails on the low PDF values as it has not been exposed to these values during training.

Combined network outputs

The right-hand column of Figure 3 shows the ‘combined’ performance of the two networks (i.e. the performance of the chosen output of the two networks based on likelihood). Compared to the single network (left column), the performance is substantially improved, with a substantial reduction in bias shown in (j). Importantly, the method retains its performance at substantially higher R_2^* values than the single network method.

Note that the increase in parameter standard deviation at high R_2^* shown in the precision plot (o) compared to (k,l) reflects the fact that the parameter estimates in (o) are obtained from a choice of two networks which are each

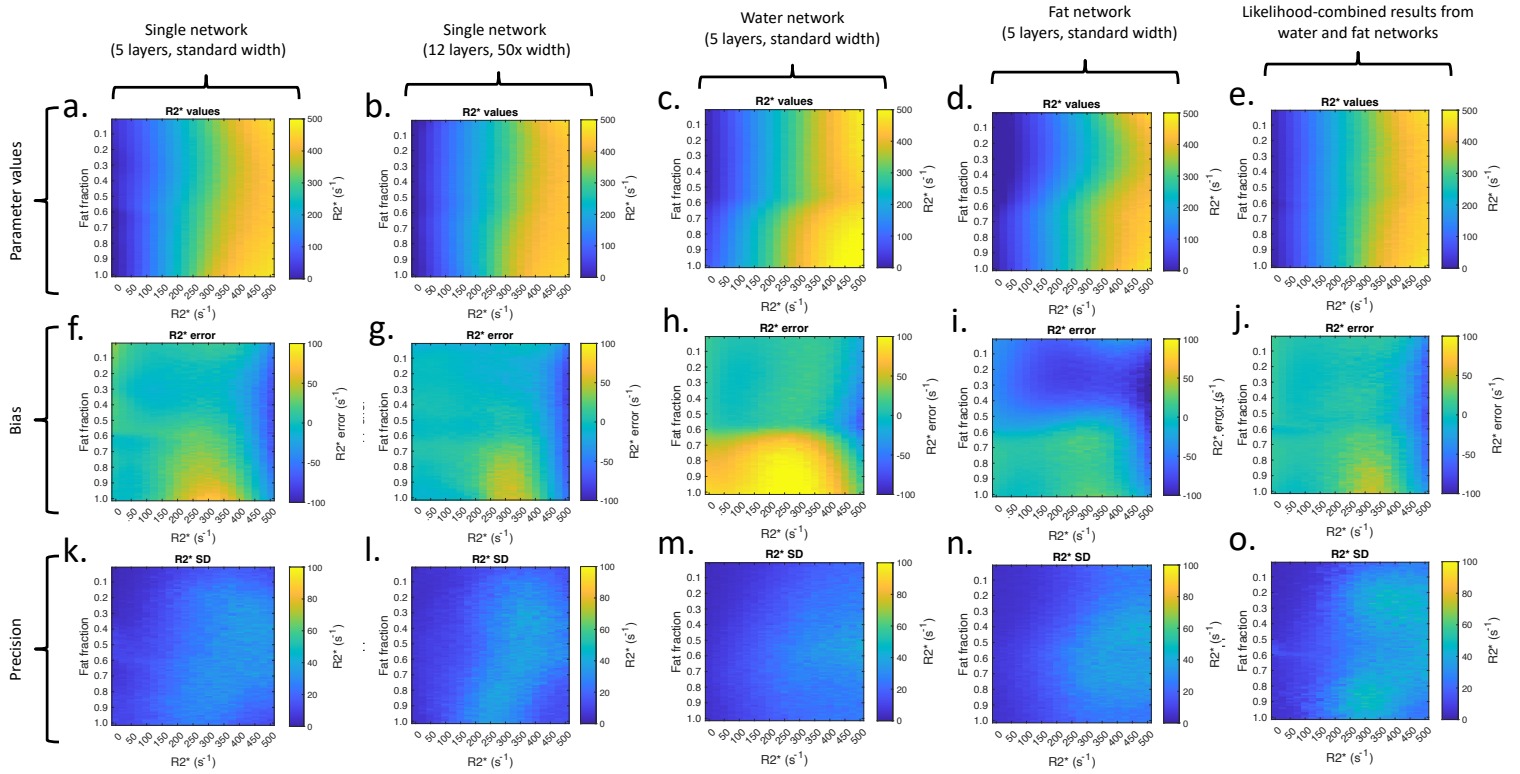


Figure 4: Improvement in R_2^* estimation for dual network approach compared to single network (evaluation in the presence of noise). The figure shows the performance of a single network with no restriction of training distribution (left and second columns, using standard and larger networks respectively), individual water and fat networks (third and fourth columns) and likelihood-combined networks (right column). The parameter values are shown on the top row, bias is displayed in the middle row and parameter standard deviation is shown on the bottom row.

accurate in their own region of parameter space, whereas those in (k,l) are consistently biased towards the middle of the PDF range across the parameter space. In other words, the pattern in (o) does not indicate poorer performance but rather the avoidance of consistently biased and less informative estimates.

Similarly, the right-hand column of Figure 4 shows the ‘combined’ performance of the two networks in terms of R_2^* estimation performance. Compared to the single network (left column and second column), the performance is slightly improved, with a reduction in bias.

Comparison with conventional fitting

Figure 5 shows the combined performance of the two networks in terms of PDF bias and precision, compared against conventional fitting in the presence of noise. The performance of RAIDER is superior to conventional fitting with MAGORINO.

This figure also shows the combined performance of the two networks in terms of R_2^* bias and precision. Again, the performance of RAIDER is similar to that of Rician magnitude fitting (with slightly higher bias, but also substantially

improved precision, at high R_2^*).

For the full simulation experiment over 212100 signal instantiations, RAIDER inference took 3.7s, again compared to 1649s (i.e. 27 minutes) for conventional fitting (446 fold acceleration).

4.2 Phantom experiments

Results of the analysis of the multisite phantom data set are shown in Figure 6.

Median PDF values for all 11 phantom vials are plotted against reference fat fraction values for all sites, acquisition protocols, and field strengths. There is good agreement between the predictions and the reference values with minimal bias across vendors and field strengths, and the overall performance was similar for the two methods. Some small differences were observed: in particular, for protocol 2 RAIDER performed better at some sites in the pure fat (high FF) vial.

Inference for the entire set of 28 phantom datasets (one slice for each) took 47.5s (i.e. 1.7s per dataset) for RAIDER, compared to 5.1 hours (i.e. 11 minutes per

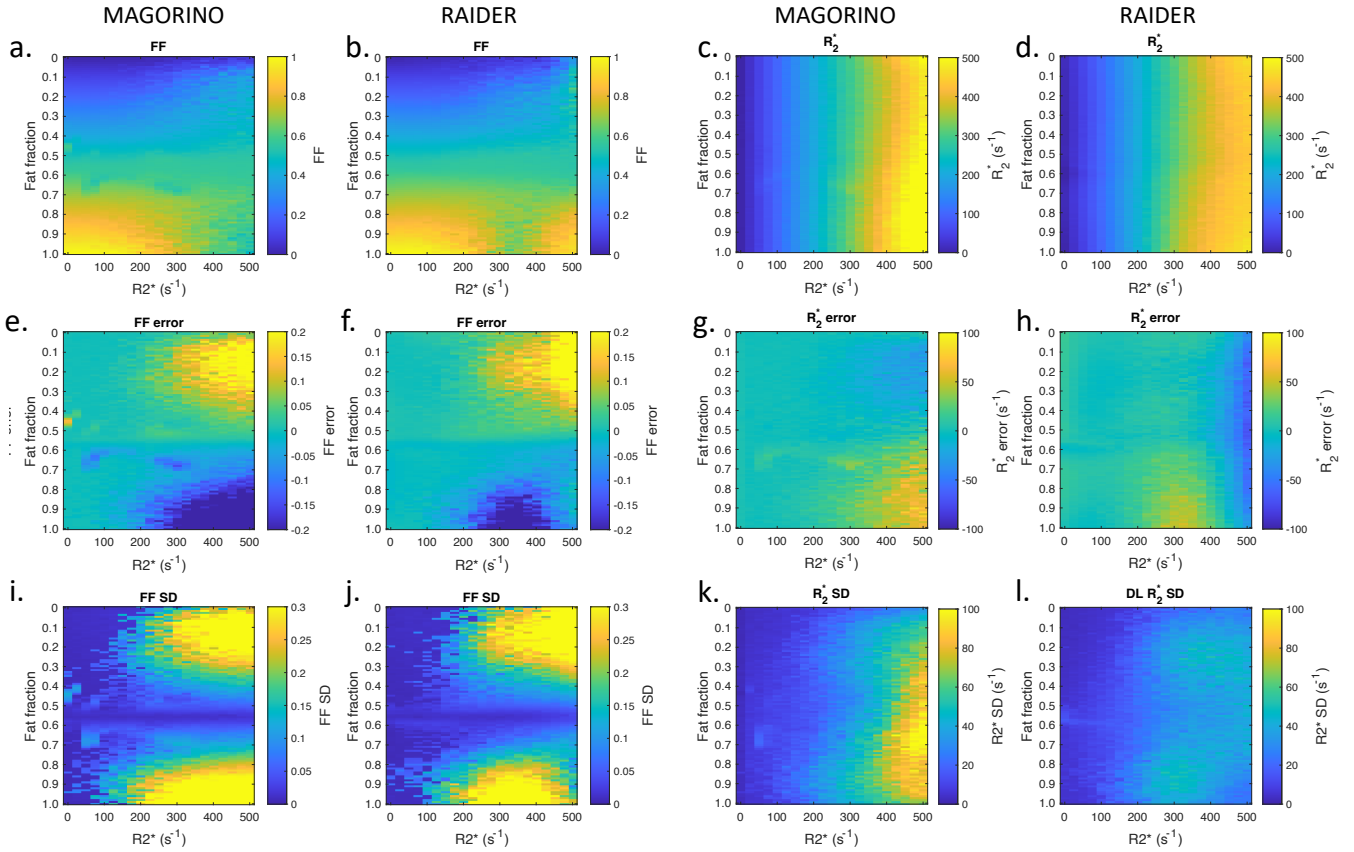


Figure 5: Performance of chosen output from two networks in the presence of noise and comparison against conventional fitting for PDFF (left two columns) and R_2^* (right two columns). The top row shows estimated parameter values, the middle row shows parameter bias, and the bottom row shows parameter variance. The first and third columns refer to conventional fitting using MAGORINO, and the second and fourth columns refer to RAIDER.

dataset) for MAGORINO (385-fold acceleration).

4.3 In vivo imaging

Example *in vivo* images are shown in Figures 7, 8 and 9. Figure 7 illustrates how the outputs from the water network (a,e) and the fat network (b,f) are combined to produce the composite predictions shown in the third column (c,g). Figure 8 and 9 includes difference maps to demonstrate differences compared to conventional fitting across multiple tissues, and scatterplots showing voxelwise differences compared to conventional fitting with MAGORINO. The RAIDER performance shown in Figures 8 and 9 was superior to that for single network predictions, where high PDFF values showed substantial negative bias similar to that observed in simulations.

Inference for the image slices shown in Figures 7 and 8 / 9 took 1.2s and 0.7s respectively, compared to 56 minutes and 17 minutes (2800-fold and 1457-fold acceleration).

5. Discussion

Recently, several groups have explored the use of magnitude-based fitting for estimating PDFF and R_2^* from chemical shift-encoded MRI data, since this approach can be used when complex-based methods fail or when phase data are inaccessible or unreliable, such as in multi-centre studies, low resource settings, preclinical imaging or when analysing large existing datasets, including biobank data. Magnitude fitting is also commonly used as a final processing step with a variety of complex-based methods. However, such methods are currently limited by their computational cost, increasing processing time and financial cost. Here, we propose RAIDER, which uses deep learning to separate water and fat in a ‘voxel-independent fashion’, performing parameter estimation separately in each voxel. The proposed method resolves a key problem with degeneracy in magnitude-based voxelwise deep learning, enabling us to unlock the potential speed advantage of single-voxel magnitude-only. Furthermore, by providing separate wa-

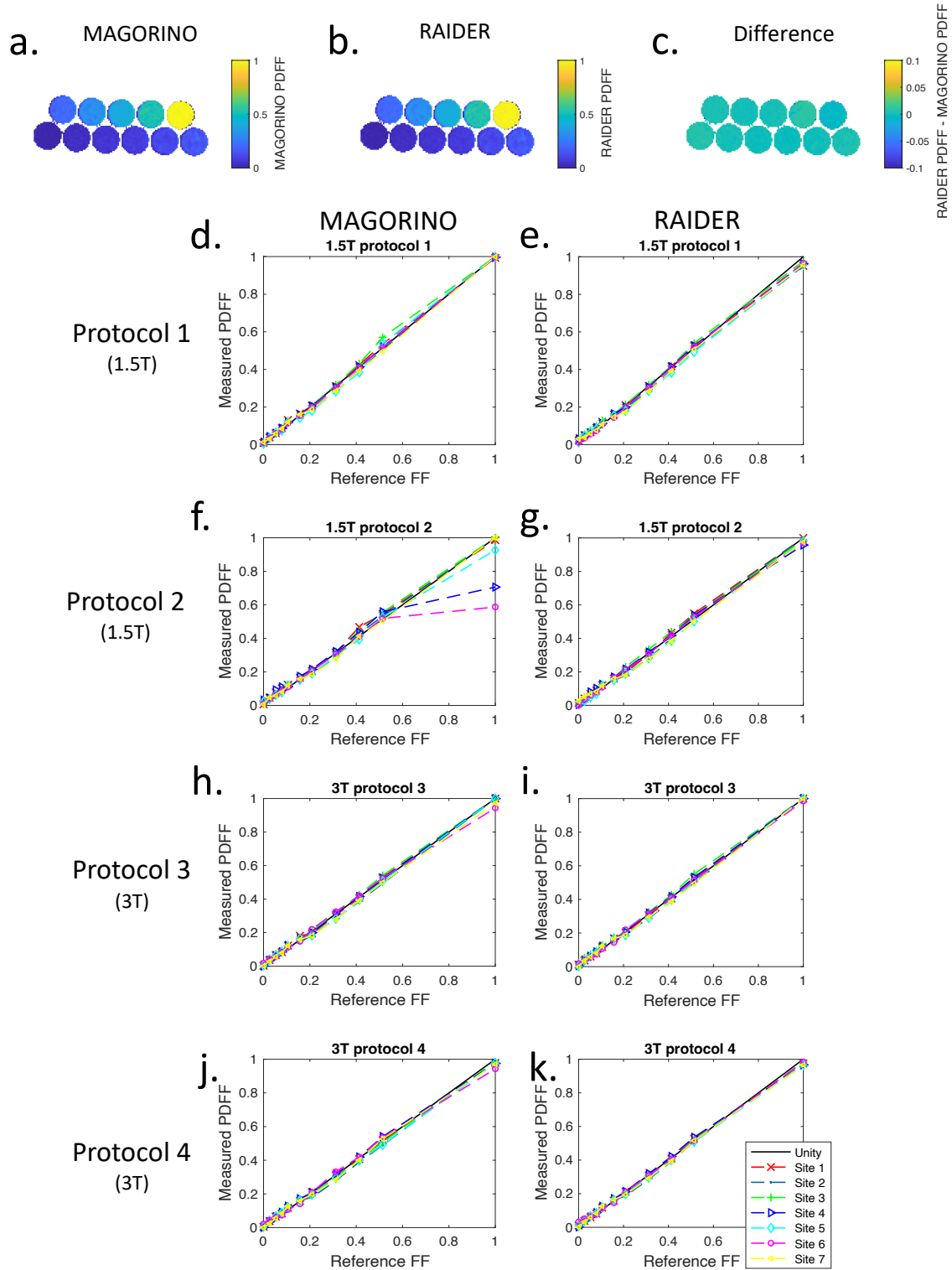


Figure 6: Results from multisite, multivendor, multi-field-strength phantom data set. Results from conventional fitting (MAGORINO) are shown in the left column, and RAIDER results are shown in the right column. Agreement plots are shown for each of the four protocols, with individual points for each of the six sites. The black 'unity' line indicates perfect agreement with reference PDFF values. "Site 7" refers to the repeat scans at site 1. The example image (top) is from site 1, 3T protocol 2, chosen to enable a direct visual comparison with corresponding illustrations in the MAGO and MAGORINO papers (Triay Bagur et al., 2018; Bray et al., 2022). Background voxels with very low signal intensity were set to white to facilitate interpretation. Reference FF values in the phantom were 0.026, 0.053, 0.079, 0.105, 0.157, 0.209, 0.312, 0.413, 0.514 and 1.

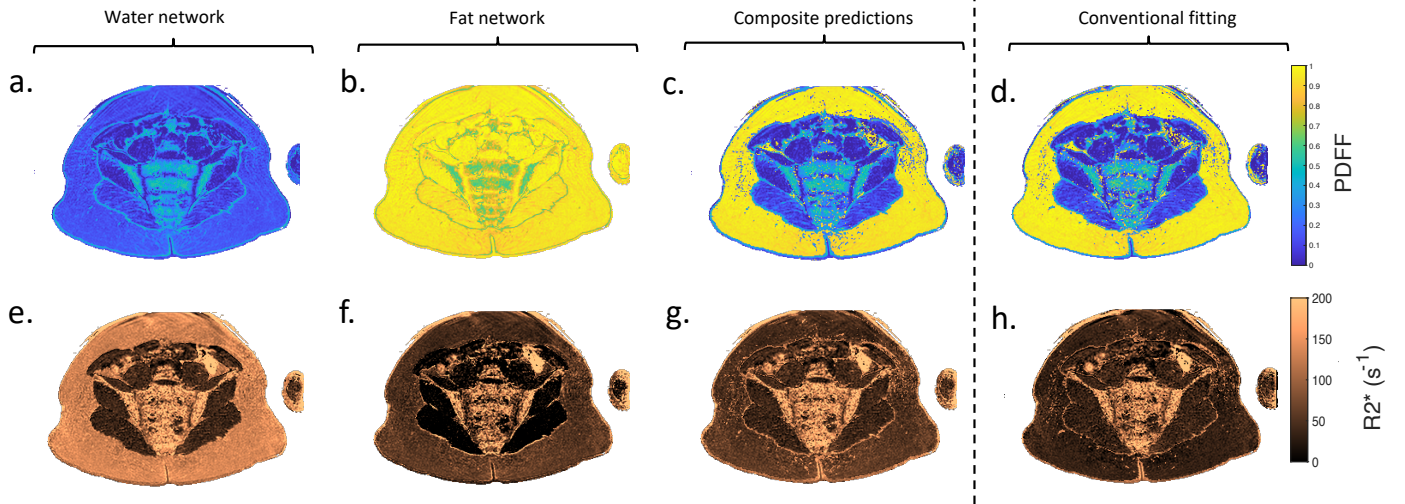


Figure 7: PDFF maps (top row) and R_2^* maps (bottom row) from the pelvis of a volunteer. Note that the water network (first column) produces exclusively low PDFF estimates whereas the fat network (second column) produces exclusively high PDFF estimates. However, the chosen output from the two networks based on likelihood (third column) produces plausible predictions across a range of tissue types, including adipose tissue (almost pure fat), muscle (almost pure water) and bone marrow (approximately equal fat and water content). These agree closely with conventional fitting performed using MAGORINO (fourth column).

ter and fat networks, the RAIDER networks also enables the use of DL-based magnitude fitting to refine predictions of other methods within a multistep process, as is commonly done with conventional magnitude fitting (Zhong et al., 2014; Hernando et al., 2017), since the appropriate network (fat or water) could be chosen depending on the output of the previous step.

The proposed RAIDER approach, using two networks with separate training data distribution design, is motivated by our demonstration that using a single network with a full training distribution, including all plausible PDFF and R_2^* values, produces relatively poor performance, with substantial bias in PDFF estimates. Furthermore, the observation that parameter estimates are biased towards the mean (typically producing intermediate fat fraction values in voxels with high fat PDFF or low PDFF ground truths) is a strong indication that this problem is due to degeneracy (Guerreri et al., 2023). We showed that performance could be improved by training individual networks on a restricted distribution of parameter values, specifically, by training one network only on low PDFF values (below the switching line) and another on high PDFF values (above the switching line). By selecting the most likely result from these networks, we were able to obtain predictions that outperformed a naive single network implementation across the full parameter space, both in simulations and *in vivo*. Importantly, our results suggest a promising approach to resolving degeneracy in qMRI more broadly: the proposed

method can be considered as analogous to methods using multiple start points in conventional fitting, and could be of value in any situation where this strategy is necessary to find the global optimum.

RAIDER offered similar or slightly improved performance to conventional MAGORINO fitting in terms of bias and precision, but was markedly faster, with an acceleration of 400-fold to 2800-fold. We also showed that this method could be successfully implemented in multisite, multivendor phantom data and *in vivo*. Our results suggest that the proposed method could help to reduce the time and expense associated with processing of CSE-MRI data for research and in clinical practice.

Thus far, for the purposes of fat-water separation, most authors have used convolutional neural networks, taking signals from the whole image as input, to separate fat and water (Goldfarb et al., 2019; Andersson et al., 2019; Jafari et al., 2021; Liu et al., 2021). These methods exploit the spatial relationships in the image as well as the information contained within individual voxels in the echo dimension, and typically use complex data. In addition to the need for complex data, these methods have other disadvantages: in particular, training is typically performed on real images from a specific anatomical region (with a particular resolution), meaning that large, expensive datasets are typically required to achieve satisfactory real-world performance. Furthermore, methods trained in this way are very unlikely to be fully generalizable to other regions of

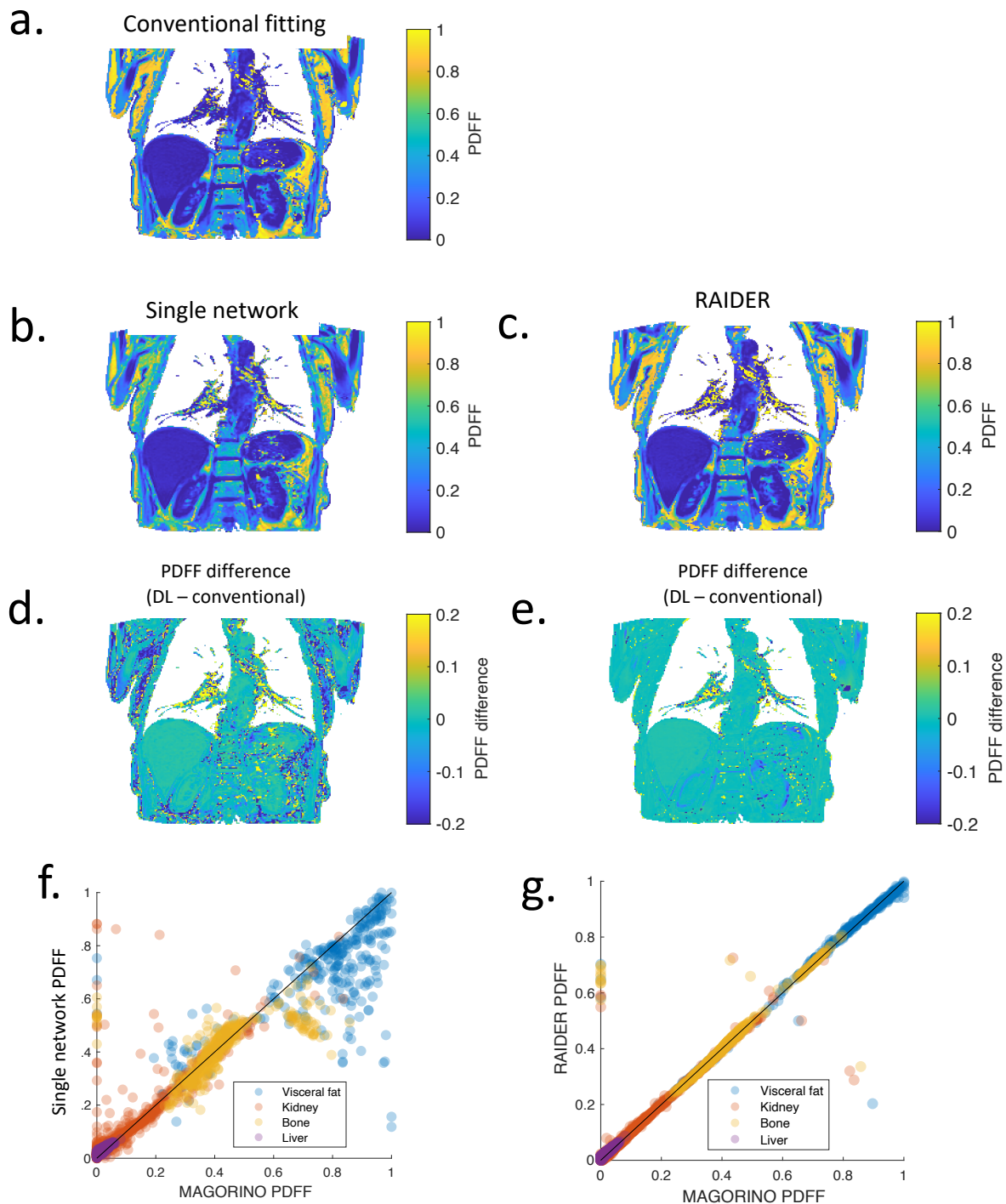


Figure 8: PDFF images of the thorax and abdomen. PDFF maps using conventional fitting (a), a single network DL implementation (b) and RAIDER (c) are shown. Difference maps between the single network approach and conventional fitting (d) and between RAIDER and conventional fitting (e), as well as scatterplots showing differences in key tissues (f,g) are also shown. For the single network method, there is substantial negative bias in the visceral fat and in the higher PDFF voxels in the bone marrow, matching the pattern expected from simulation; this error is substantially reduced for RAIDER. The precision of RAIDER estimates is also superior to that from the single network method. Note that very low signal voxels in the background were masked out and are displayed as white to increase the clarity of the images.

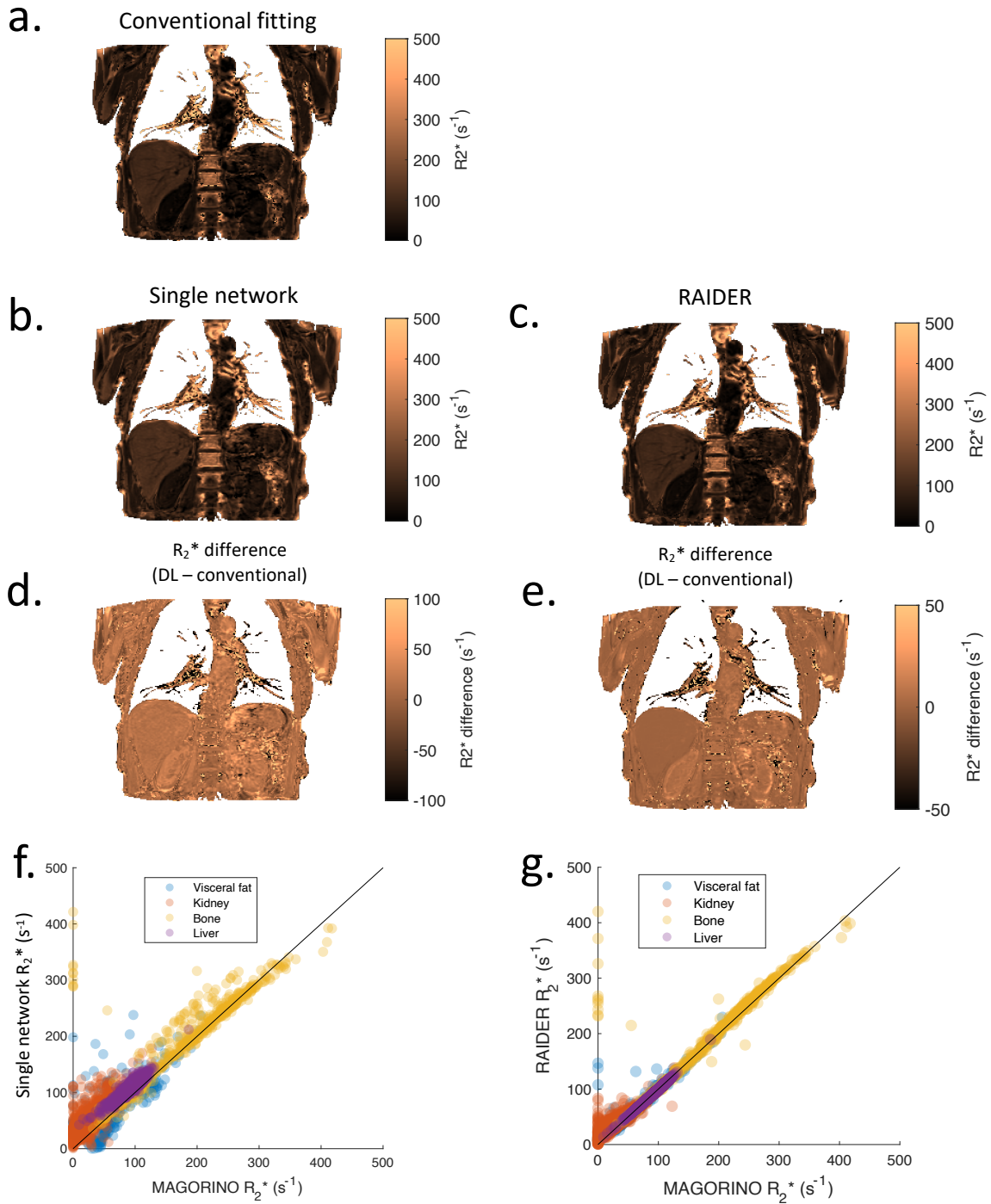


Figure 9: R_2^* images of the thorax and abdomen in the same volunteer as in Figure 8. R_2^* maps using conventional fitting (a), a single network DL implementation (b) and RAIDER (c) are shown. Difference maps between the single network approach and conventional fitting (d) and between RAIDER and conventional fitting (e), as well as scatterplots showing differences in key tissues (f,g) are also shown. For the single network method, there is greater positive bias at low R_2^* than for RAIDER, matching the pattern expected from simulation. The precision of RAIDER estimates is also superior to that from the single network method; this is particularly pronounced for the bone marrow (an intermediate PDF, high R_2^* tissue), again matching the pattern seen in simulation. Note that very low signal voxels in the background were masked out and are displayed as white to increase the clarity of the images.

the body or to pathological cases that they have not been trained on. CNN-based methods are also highly vulnerable to differences in acquisition parameters such as image matrix, and training networks using this approach is typically extremely slow, with training taking many hours or even days (Goldfarb et al., 2019; Andersson et al., 2019; Jafari et al., 2021; Liu et al., 2021). In contrast, voxel-independent methods (Barbieri et al., 2019; Epstein et al., 2024; Gyori et al., 2021) have the advantage that there is no inherent dependence on anatomy, pathology or acquisition geometry introduced during training, making them potentially much more generalizable across anatomical regions, clinical applications and scan geometries.

In this implementation, separate networks are required for different echo schemes, however, these networks can be trained relatively fast (using entirely simulated data, with no need for acquiring real data from many individuals) and are also compact, meaning that multiple versions of a model could very easily be stored on a scanner, having been trained in advance. This is a clear advantage over CNN-based methods, where different acquisition schemes will require new training data (which is orders of magnitude more expensive and difficult to obtain). Furthermore, RAIDER could potentially be extended by using methods such as neural controlled differential equations (Kuppens et al., 2024) to remove the need for re-training with different acquisition settings.

Further work is required to investigate the relative strengths and weaknesses of different deep learning-based methods, and to consider how hybrid approaches (for example, combining deep learning and conventional fitting methods) might be used to balance speed and performance. Overall, the potential acceleration offered by deep learning-based methods offers to substantially accelerate and simplify PDFF and R_2^* estimation.

This work has some limitations. Firstly, under optimal conditions where the phase is completely reliable, the performance of magnitude-based methods, including the proposed RAIDER method as well as the existing MAGO and MAGORINO methods, is likely to be inferior to complex-based methods as well as more sensitive to model mismatch (Hernando et al., 2010; Wang et al., 2016). However, this class of methods is explicitly designed for situations where the phase is unavailable or unreliable, and for refining initial estimates produced by complex signal-based methods. As described in the Introduction, such magnitude-based approaches are used in a variety of settings and increasingly seen as a practical and generalizable method. Secondly, this is a 'proof-of-concept' study, describing a new methodological approach, and the evaluation with real data is preliminary. Thirdly, in its present form the method may be vulnerable to domain shift, for example in tissues with low proton density or very high R_2^* which are not encountered

in the training data. This could be addressed by incorporating alternative DL approaches such as the self-supervised learning approach proposed by Barbieri et al. (2019). However, for most existing clinical applications this is of little concern, as the training method can easily be tailored to the tissues in question. Fourthly, the current implementation produced slightly biased R_2^* estimates in subcutaneous fat, likely because the single peak normalization procedure (see 3.1.1) is imperfect and can result in more inaccurate S_0 estimates in this tissue due to fat-fat interference; this issue may be addressed by developing improved normalization strategies. Finally, the choice of the 'switching point' is currently partly empirical (based on an understanding of the objective function shown in Figure 1), and there is scope for developing an analytical method for determining the precise value of this point. However, we expect that small changes in the switching point will have little effect on performance.

6. Conclusions

We propose RAIDER, a voxelwise method for rapid, anatomy-independent deep learning-based $Pdff$ and R_2^* estimation using multi-echo magnitude-data. RAIDER utilises two neural networks, each with a separately-designed training data distribution, to deal with degeneracy and thus realise the acceleration offered by an MLP-based approach, namely a 400-fold to 2800-fold acceleration. This means that processing takes just seconds, rather than minutes or hours.

Acknowledgments

TJPB and MHC received personal support by the UCLH National Institute for Health Research Biomedical Research Centre (NIHR BRC); TJPB was also supported by NIHR BRC grants BRC1122/HEI/JP/110410 and BRC1185/III/TB/101350. This work was undertaken at UCLH/UCL, which receives funding from the UK Department of Health's NIHR BRC funding scheme. The funders had no role in study design, data collection and analysis, decision to publish, or preparation of the manuscript.

Ethical Standards

The work follows appropriate ethical standards in conducting research and writing the manuscript, following all applicable laws and regulations regarding treatment of animals or human subjects.

Conflicts of Interest

We declare we don't have conflicts of interest.

Data availability

The code for RAIDER implementation is available at <https://github.com/TJPBray/DixonDL>. The code used to generate the results in this paper are preserved in their original form as release v1.0.

Appendix A. Noise-free results

Results for a noise-free version of the experiments in Section 3.2 are provided in Figure 10.

Appendix B. Learning curves

Key training curves for the experiments performed in 3.2 and in Appendix A are provided in Figure 11.

References

- J Andersson, H Ahlström, and J Kullberg. Separation of water and fat signal in whole-body gradient echo scans using convolutional neural networks. *Magn Reson Med*, 82:1177–1186, 2019.
- A Bainbridge, TJP Bray, R Sengupta, and MA Hall-Craggs. Practical approaches to bone marrow fat fraction quantification across magnetic resonance imaging platforms. *Journal of Magnetic Resonance Imaging*, 2020.
- S Barbieri, O Gurney-Champion, R Klaassen, and H Thoeney. Deep learning how to fit an intravoxel incoherent motion model to diffusion-weighted MRI. *Magn Reson Med*, 83(1):312–321, 2019.
- CM Bishop and CM Roach. Fast curve fitting using neural networks. *Rev Sci Instrum*, 63(10):4450–4456, 1992.
- TJP Bray, A Bainbridge, S Punwani, Y Ioannou, and MA Hall-Craggs. Simultaneous quantification of bone edema/adiposity and structure in inflamed bone using chemical shift-encoded MRI in spondyloarthritis. *Magn Reson Med*, 79(2):1031–1042, 2018a.
- TJP Bray, MD Chouhan, S Punwani, A Bainbridge, and MA Hall-Craggs. Fat fraction mapping using magnetic resonance imaging: insight into pathophysiology. *Br J Radiol*, 91:1089, 2018b.
- TJP Bray, A Bainbridge, MA Hall-Craggs, and H Zhang. MAGORINO: Magnitude-only fat fraction and R2* estimation with Rician noise modelling. *Magn Reson Med*, 89:1173–1192, 2022.
- V Choida, A-V Madenidou, D Sen, MA Hall-Craggs, and C Ciurtin. The role of whole-body MRI in musculoskeletal inflammation detection and treatment response evaluation in inflammatory arthritis across age: A systematic review. *Semin Arthritis Rheum*, 52:151953, 2022.
- V Choida, TJP Bray, Niels van Vucht, MA Abbasi, A Bainbridge, T Parry, D Sen, S Mallett, C Ciurtin, and MA Hall-Craggs. Detection of inflammation by whole-body mri in young people with juvenile idiopathic arthritis. *Rheumatology*, 63:S1207–214, 2024.
- DA Clevert, T Unterthiner, and S Hochreiter. Fast and accurate deep network learning by exponential linear units (ELUs). *arXiv*, page 1511.07829, 2015.
- German National Cohort Consortium. The german national cohort: aims, study design and organization. *Eur J Epidemiol*, 29:371–82, 2014.
- CM Costelloe, V Kundra, J Ma, BA Chasen, EM Rohren, RL Bassett, and JE Madewell. Fast Dixon whole-body MRI for detecting distant cancer metastasis: a preliminary clinical study. *J Magn Reson Imaging*, 35(2):399–408, 2012.
- S Epstein, TJP Bray, MA Hall-Craggs, and H Zhang. Choice of training label matters: how to best use deep learning for quantitative MRI parameter estimation. *J Mach Learn Biomed Imaging*, 2:586–610, 2024.
- H Ghimire, M Malekzadeh, JE Lim, SS Madabush, MA Zampini, A Camacho, W Hu, G Storme, MM Al Malki, and SK Hui. Development of proton density fat fraction micro-mri for non-invasive quantitative assessment of bone marrow changes with age and radiation in mouse models. *arXiv*, 2025.
- JW Goldfarb, J Craft, and JJ Cao. Water–fat separation and parameter mapping in cardiac MRI via deep learning with a convolutional neural network. *J Magn Reson Imag*, 50:655–665, 2019.
- V Golkov, JI Dosovitskiy, A Speri, MI Menzel, M Czisch, P Samann, T Brox, and D Cremers. q-space deep learning: Twelve-fold shorter and model-free diffusion mri scans. *IEEE Trans Med Imaging*, 35(5):1344–1351, 2016.
- M Guerreri, S Epstein, H Azadbakht, and H Zhang. Resolving quantitative MRI model degeneracy with machine learning via training data distribution design. *Inf Process Med Imaging*, 2023.
- N Gyori, M Palombo, CA Clark, H Zhang, and DC Alexander. Training data distribution significantly impacts the estimation of tissue microstructure with machine learning. *Magn Reson Med*, page 29014, 2021.
- D Hernando, JP Haldar, J Ma, P Kellman, and Z-P Liang. Joint estimation of water/fat images and field inhomogeneity map. *Magn Reson Med*, 59(3):571–80, 2008.
- D Hernando, Z-P Liang, and P Kellman. Chemical shift-based water/fat separation: A comparison of signal models. *Magn Reson Med*, 64:811–822, 2010.
- D Hernando, SD Sharma, MA Ghasabeh, BD Alvis, SS Arora, G Hamilton, L Pan, and JM Shaffer. Multisite,

- multivendor validation of the accuracy and reproducibility of proton-density fat-fraction quantification at 1.5T and 3T using a fat–water phantom. *Magn Reson Med*, 77:1516–1524, 2017.
- R Jafari, P Spincemaille, J Zhang, TD Nguyen, X Luo, J Cho, D Margolis, MR Prince, and Y Wang. Deep neural network for water/fat separation: Supervised training, unsupervised training, and no training. *Magn Reson Med*, 85:2253–2277, 2021.
- D Karimi. Diffusion mri with machine learning. *Imaging Neuroscience*, 2(2):1–55, 2024.
- JP Kuhn, F Berthold, J Mayerle, H Volzke, SB Reeder, W Rathman, MM Lerch, N Hosten, K Hegenscheid, and PJ Meffert. Pancreatic steatosis demonstrated at MR imaging in the general population: clinical relevance. *Radiology*, 276(1):129–136, 2015.
- D Kuppens, S Barbieri, D van den Berg, P Schouten, HC Thoeny, M Wennen, and OJ Gurney-Champion. Acquisition-independent deep learning for quantitative mri parameter estimation using neural controlled differential equations. *arXiv*, page 2412.20844, 2024.
- A Latifoltojar, MA Hall-Craggs, A Bainbridge, N Rabin, R Popat, A Rismani, S D’Sa, N Dikaois, M Sokolsa, M Antonelli, S Ourselin, K Yong, SA Taylor, S Halligan, and S. Punwani. Whole-body MRI quantitative biomarkers are associated significantly with treatment response in patients with newly diagnosed symptomatic multiple myeloma following bortezomib induction. *Eur Radiol*, 27(12):5325–5336, 2017.
- TJ Littlejohns, J Holliday, LM Gibson, S Garratt, N Oesingmann, F Alfaro-Almagro, JD Bell, C Boulton, R Collins, MC Conroy, N Crabtree, N Doherty, AF Frangi, NC Harvey, P Leeson, KL Miller, S Neubauer, SE Peteresen, J Sellors, S Sheard, SN Smith, CLM Sudlow, PM Matthrs, and NE Allen. The uk biobank imaging enhancement of 100,000 participants: rationale, data collection, management and future directions. *Nature Communications*, 11, 2020.
- CY Liu, CA McKenzie, H Yu, JH Brittain, and SB Reeder. Fat quantification with IDEAL gradient echo imaging: Correction of bias from T1 and noise. *Magn Reson Med*, 58(2):354–64, 2007.
- K Liu, Xiaojun Li, Y Chen, H Xiong, F Chen, Qinjia Bao, and C Liu. Robust water–fat separation based on deep learning model exploring multi-echo nature of mGRE. *Magn Reson Med*, 85:2828–2841, 2021.
- V Losev, C Lu, DS Senevirathne, P Inglese, W Bai, AP King, M Shah, A de Marvao, and DP O’Regan. Body fat and human cardiovascular ageing. *medRxiv*, 2024.
- A Mastropietro, D Procissi, E Scalco, G Rizzo, and N Bertolino. A supervised deep neural network approach with standardized targets for enhanced accuracy of ivim parameter estimation from multi-snr images. *NMR in Biomedicine*, 35(10):e4774, 2019.
- C Messiou, J Hillengass, S Delorme, F Lecouvet, L Mouloupoulos, DJ Collins, MD Blackledge, N Abildgaard, B Ostergaard, HP Schlemmer, O Landgren, JT Asmussen, MF Kaiser, and A. Padhani. Guidelines for acquisition, interpretation, and reporting of whole-body mri in myeloma: Myeloma response assessment and diagnosis system (my-rads)n. *Radiology*, 291(1), 2019.
- JM Morrow, CDJ Sinclair, A Fischmann, P Machado, MM Reilly, TA Yousry, JS Thornton, and MG Hanna. MRI biomarker assessment of neuromuscular disease progression: a prospective observational cohort study. *Lancet Neurol*, 15(1):65–77, 2016.
- S Murali, H Ding, F Adedeji, C Qin, J Obungoloch, I Asllani, U Anazado, NAB Ntusi, R Mammen, T Nien-dorf, and S Adeleke. Bringing mri to low- and middle-income countries: Directions, challenges and potential solutions. *NMR in Biomedicine*, 37:e4992, 2022.
- M Nouredin, J Lam, MR Petereson, M Middleton, G Hamilton, T-A Le, R Betterncourt, C Changchien, DA Brenner, C Sirlin, and R Loomba. Utility of magnetic resonance imaging versus histology for quantifying changes in liver fat in nonalcoholic fatty liver disease trials. *Magn Reson Med*, 58(6):1930–1940, 2013.
- SB Reeder, Z Wen, H Yu, AR Pineda, GE Gold, M Markl, and NJ Pelc. Multicoil Dixon chemical species separation with an iterative least-squares estimation method. *Magn Reson Med*, 51(1):35–45, 2004.
- SB Reeder, AR Pineda, Z Wen, A Shimakawa, H Yu, JH Brittain, GE Gold, CH Beaulieu, and NJ Pelc. Iterative decomposition of water and fat with echo asymmetry and least-squares estimation (IDEAL): Application with fast spin-echo imaging. *Magn Reson Med*, 54(3): 636–644, 2005.
- SA Taylor, SM Mallett, S Beare, G Bhatnagar, D Blunt, P Boavida, J. Bridgewater, et al. Diagnostic accuracy of whole-body MRI versus standard imaging pathways for metastatic disease in newly diagnosed colorectal cancer: the prospective Streamline C trial. *Lancet Gastro Hep*, 4(7):529–537, 2019.

- A Triay Bagur, C Hutton, B Irving, ML Gyngell, MD Robson, and M Brady. Magnitude-intrinsic water–fat ambiguity can be resolved with multipeak fat modeling and a multipoint search method. *Magn Reson Med*, 82(1): 460–475, 2018.
- A Triay Bagur, D McClymont, C Hutton, A Borghetto, ML Gyngell, P Alijabar, MD Robson, M Brady, and DP Bulte. Estimation of field inhomogeneity map following magnitude-based ambiguity-resolved water-fat separation. *Magn Reson Imag*, 97:102–111, 2023.
- T Waddell, A Bagur, D Cunha, H Thomaides-Brears, R Banerjee, DJ Cuthbertson, E Brown, K Cusi, JP Despres, and M Brady. Greater ectopic fat deposition and liver fibroinflammation and lower skeletal muscle mass in people with type 2 diabetes. *Obesity*, 30:1231–1238, 2022.
- X Wang, D Hernando, and SB Reeder. Sensitivity of chemical shift-encoded fat quantification to calibration of fat MR spectrum. *Magn Reson Med*, 75:845–851, 2016.
- WJ Wong, C Emdin, AG Bick, SM Zekavat, A Niroula, JP Pirruccello, L Dichtel, G Griffin, MM Uddin, CJ Gibson, V Kovalcik, AE Lin, ME McConkey, A Vroman, RS Sellar, PG Kim, M Agrawal, J Weinstock, MT Long, B Yu, R Banerjee, RC Nicholls, A Dennis, M Kelly, PR Loh, S McCarroll, E Boerwinkle, RS Vasan, S Jaiswal, AD Johnson, RT Chung, K Corey, D Levy, C Ballantyne, BL Ebert, and Natarajan P. Clonal haematopoiesis and risk of chronic liver disease. *Nature*, 616:747–754, 2023.
- JH Yoon, JM Lee, KB Lee, SW Kim, MJ Kang, JY Jang, S Kannengiesser, JK Han, and BI Choi. Pancreatic steatosis and fibrosis: quantitative assessment with pre-operative multiparametric MR imaging. *Radiology*, 279: 140–150, 2016.
- X Zhong, MD Nickel, SA Kannengiesser, BM Dale, B Kiefer, and MR Bashir. Liver fat quantification using a multi-step adaptive fitting approach with multi-echo GRE imaging. *Magn Reson Med*, 72:1353–1365, 2014.

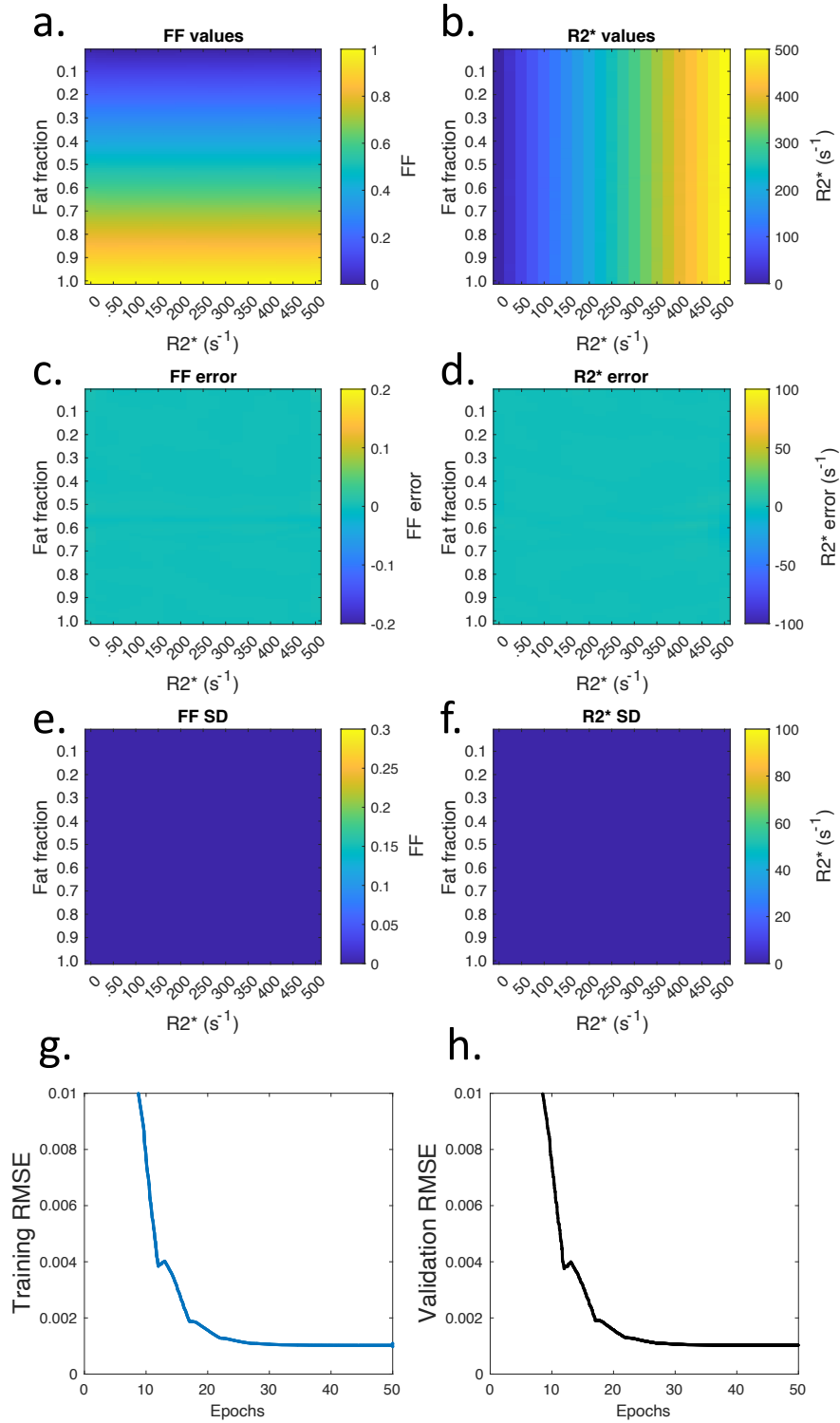


Figure 10: Performance of the larger single network (12 layers, 50x width) in with noise-free training and testing. There is very little error across the entire parameter space, indicating that (i) there is minimal true degeneracy without noise and (ii) the network has sufficient capacity to describe the tissue model. The training curve for this network is displayed with very narrow y axis limits to show that there is no under or overfitting (this is the same curve as in the bottom left pane of Figure 11).

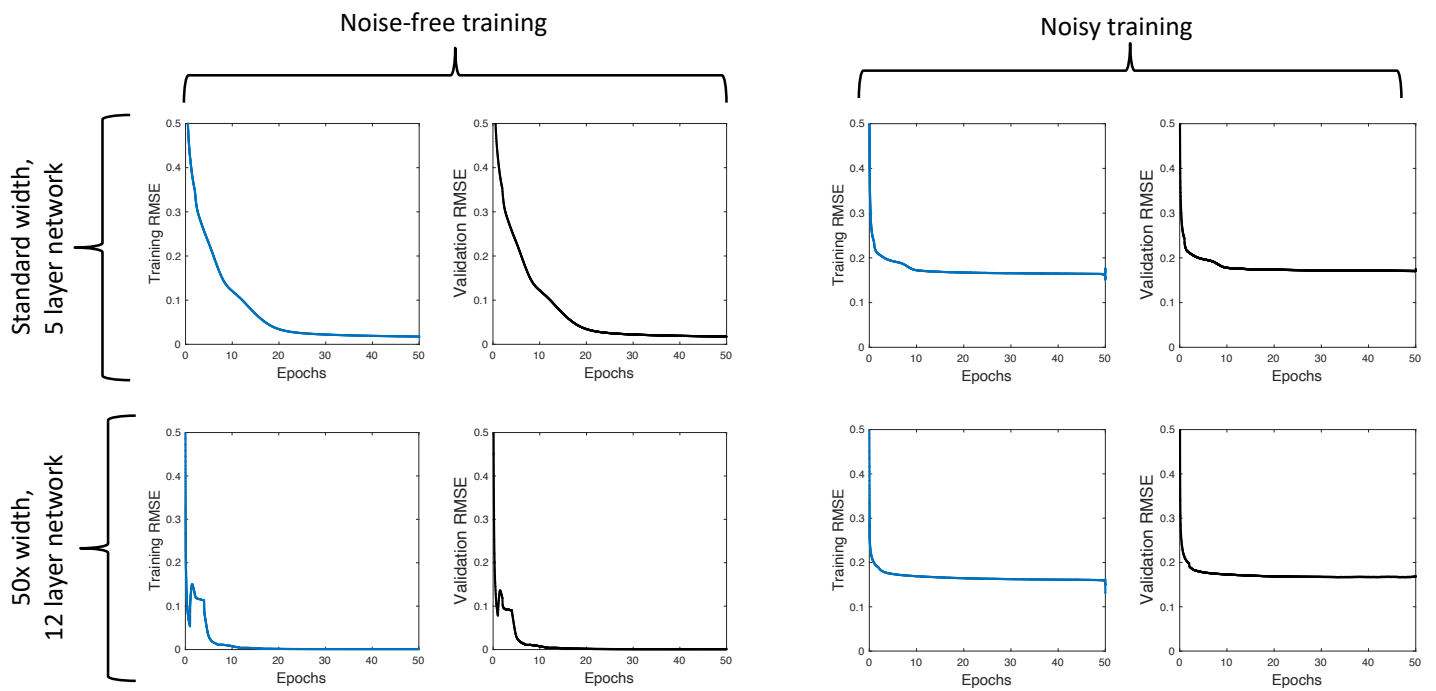


Figure 11: Training curves for standard width networks (top row) and larger networks (bottom row), with noise free data (left column) and with noisy data (right column). The training curve for the bottom left plots correspond to the performance plots shown in 10; the two plots in the right column correspond with the smaller and larger single networks whose performance is shown in 3 and 4 (first two columns of both figures). The performance plots for the top left training curves are not shown; this was slightly poorer than for the results in 10, in keeping with the higher RMSE on the training curves.